ADVANCING EARTH AND SPACE SCIENCES

JGR Planets

RESEARCH ARTICLE

10.1029/2024JE008916

Water Vapor Vertical Distribution on Mars After Six Years of TGO/NOMAD Solar Occultations: 1. Global Climatology

A. Brines[1], M. A. López-Valverde[1], B. Funke[1], F. González-Galindo[1], S. Aoki[2,3], I. R. Thomas[2], G. L. Villanueva[4], G. Liuzzi[5], J. T. Erwin[2], U. Grabowski[6], F. Forget[7], J. J. Lopez-Moreno[1], J. Rodriguez-Gomez[1], F. Daerden[2], L. Trompet[2], B. Ristic[2], M. R. Patel[8], J. A. Holmes[8], G. Bellucci[9], A. Modak[10], and A. C. Vandaele[2]

[1]Instituto de Astrofísica de Andalucía (IAA/CSIC), Granada, Spain, [2]Royal Belgian Institute for Space Aeronomy, Brussels, Belgium, [3]Department of Complexity Science and Engineering, University of Tokyo, Tokyo, Japan, [4]NASA Goddard Space Flight Center, Greenbelt, MD, USA, [5]University of Basilicata, Potenza, Italy, [6]Karlsruhe Institute of Technology, Institute of Meteorology and Climate Research, Karlsruhe, Germany, [7]Laboratoire de Météorologie Dynamique, IPSL, Paris, France, [8]Open University, Milton Keynes, UK, [9]Istituto di Astrofisica e Planetologia, Rome, Italy, [10]Institute for Basic Science, Daejeon, South Korea

Key Points:

- Three complete Martian Years of water vapor vertical distribution from Mars' troposphere to mesopause using infrared solar occultations
- More vertically extended water vapor abundances during perihelion seasons compared to aphelion as a result of Mars' orbital eccentricity
- Water vapor morning enhancement at high altitudes in the northern hemisphere during the local winter

Correspondence to:

A. Brines,
adrianbm@iaa.es

Citation:

Brines, A., López-Valverde, M. A., Funke, B., González-Galindo, F., Aoki, S., Thomas, I. R., et al. (2026). Water vapor vertical distribution on Mars after six years of TGO/NOMAD solar occultations: 1. Global climatology. *Journal of Geophysical Research: Planets*, *131*, e2024JE008916. https://doi.org/10.1029/2024JE008916

Received 20 DEC 2024
Accepted 12 MAY 2025

Author Contributions:

Conceptualization: A. Brines
Data curation: A. Brines
Formal analysis: A. Brines
Investigation: A. Brines, M. A. López-Valverde, F. González-Galindo
Methodology: A. Brines
Project administration: M. A. López-Valverde, F. González-Galindo
Software: A. Brines, B. Funke, F. González-Galindo
Supervision: M. A. López-Valverde
Validation: M. A. López-Valverde
Writing – original draft: A. Brines
Writing – review & editing: M. A. López-Valverde

Abstract We present vertical profiles of water vapor obtained during six continuous years of solar occultation observations in the infrared by the Nadir and Occultation for MArs Discovery (NOMAD) instrument on board Trace Gas Orbiter. The retrievals have been performed with an inversion code previously applied to smaller samples of this data set, but improved to combine pairs of diffraction orders allowing for sounding water vapor up to about 120 km altitude. As a first part of a set of two papers, this study presents the most extended data set of water vapor measurements from the NOMAD instrument to date, covering three full and consecutive Martian Years. Building upon previous researches primarily focused on the perihelion season, this analysis now includes the aphelion season, offering a comprehensive view of Mars' water cycle. Observations from April 2018 to December 2023 were analyzed, covering perihelion of Mars Year (MY) 34 to aphelion of MY 37 and presenting water vapor vertical profiles from approximately 5–10 km to 110–120 km in altitude. This study reveals consistent seasonal and latitudinal water vapor patterns, showing water vapor systematically more vertically extended during the perihelion season than during the aphelion. We present an extensive analysis of the water vapor local time variability, confirming overall larger abundances during the evenings than during mornings. These data provide new insights into the vertical distribution of atmospheric water vapor on Mars, aiding future comparisons and global climate model validation.

Plain Language Summary Here we study water vapor in Mars' atmosphere, a key element for understanding the planet's climate and its evolution from a once warmer, wetter world to the cold, dry planet it is today. Although Mars currently has relatively small amounts of water vapor in the atmosphere, this vapor significantly influences surface and atmospheric processes, shaping the planet's complex water cycle. Using the Nadir and Occultation for MArs Discovery (NOMAD) instrument on the Trace Gas Orbiter, we analyzed infrared spectra taken from April 2018 to December 2023, spanning different seasons and times of day over three complete Martian years. We found that water vapor extends to higher altitudes during Mars' warmer season compared to the colder season. Additionally, water vapor was generally more abundant during the evenings than in the mornings. This work presents the most extensive data set on Mars' water vapor vertical distribution, providing a more comprehensive view of how water vapor varies across time and location on the planet.

1. Introduction

Among many other open research fields, the presence of water vapor in the Martian atmosphere stands out as a particularly engaging topic of study. This species on Mars, despite its relative low abundance, provides critical clues about the planet's climate. Water vapor participates actively on many surface and atmospheric processes such as regolith-atmosphere interactions, chemistry and photochemistry, nucleation, sublimation and transport. Its distribution throughout the planet depends, directly or indirectly, on those processes resulting in a complex water cycle also strongly coupled with temperature variations, and therefore, on the atmospheric dynamics at local and global scales. Understanding the dynamics, sources, and variability of water vapor in the Martian atmosphere nowadays and through time is essential for piecing together the planet's geological and atmospheric

10.1029/2024JE008916

evolution, which has driven Mars from a more humid and warmer past to the colder and dryer planet we observe today. Despite its importance, the knowledge about the vertical distribution of water vapor in the Martian atmosphere was limited until recent years. Most of the information about water vapor available today comes from nadir sounders like the Thermal Emission Spectrometer onboard Mars Global Surveyor (Smith, 2002, 2004) and models (Forget et al., 1999; Haberle et al., 2019). The description of water vapor in the vertical was very necessary but it requires limb sounding capabilities, and ideally, a solar occultation strategy, widely used on Earth for atmospheric sounding. This technique has allowed us to achieve sensitivities high enough to study the precise vertical distribution of water vapor, among other trace species.

The first solar occultations on Mars focused on water vapor were performed by the Auguste experiment during the Phobos mission (Rodin et al., 1997). They reported vertical profiles during northern spring equinox, showing a sharp decrease in abundance above 25 km and confirming the presence of a hygropause at 30 km. Mars experiences significant changes in temperature and pressure with latitude and season, which affects the sublimation-condensation of water ice and the vertical and meridional transport of water vapor. This variability means that a comprehensive understanding of the water cycle requires continuous and systematic monitoring over extended periods, a milestone that could not be achieved with short-term missions.

The Spectroscopy for the Investigation of the Characteristics of the Atmosphere of Mars (SPICAM) onboard Mars Express was the first instrument in orbit around Mars with the ability to systematically use the solar occultation technique. Early studies with this instrument provided water vapor vertical profiles from about 15 to 50 km which were used as an indicator of an atmosphere of about 5 K warmer than predictions by Global Circulation Models (GCMs) at those altitudes (Fedorova et al., 2009). In addition, SPICAM found that supersaturation (saturation ratio exceeding 1) was persistent in the Martian atmosphere during the northern spring-summer seasons, precisely during solar longitudes (L_S) ranging from 50° to 120° (Maltagliati et al., 2011). It also revealed observations-GCM discrepancies in the abundance of water above 30 km. Similar studies carried out for the full Martian Year (MY) showed the importance of the vertical distribution on the water cycle. SPICAM also reported for the first time larger abundances and more vertically extended profiles during the perihelion than during the aphelion season, which were unexpected based on the previous knowledge of column density measurements (Maltagliati et al., 2013). In addition, the analysis of observations during the MY 28 global dust storm showed that water vapor was present at altitudes up to 80 km with abundances larger than 100 ppm (Fedorova et al., 2018). More recently, Fedorova et al. (2021) presented another relevant SPICAM result, showing water vapor density profiles for MYs 28 to 34 and confirming the impact of dust storms on water vapor vertical distribution at middle and high altitudes, adding to the impact of the perihelion season on the hydrogen escape rates.

In April 2018, the Trace Gas Orbiter (TGO) started its regular science operations. With several solar occultation instruments onboard such as the Nadir and Occultation for MArs Discovery (NOMAD, (Vandaele et al., 2018)) and the Atmospheric Chemistry Suite (ACS, (Korablev et al., 2018)), the orbital configuration of TGO makes this spacecraft suitable to monitor the Martian atmosphere with an excellent sampling in the vertical and a good latitudinal and seasonal coverage. To date, many studies have been carried out with NOMAD and ACS, reporting outstanding results since the beginning of the mission revealing valuable information about the vertical structure and variability of the Martian atmosphere. To mention a few, the 2018 Global Dust Storm (GDS) was extensively discussed by several teams, confirming to have a strong impact on the water vertical distribution (Aoki et al., 2019; Brines et al., 2023; Fedorova et al., 2020; Vandaele et al., 2019). Global dust storms allow water vapor to be present at high altitudes and prevent its condensation due to the enhanced radiative heating (Neary et al., 2020). The high sensitivity of those instruments allowed for the study of water isotopic fractionation (G. L. Villanueva et al., 2022), which revealed the prevalence of the perihelion season for the formation of atomic hydrogen and deuterium at high altitudes (Alday et al., 2021). Also, a few recent studies devoted to the perihelion season characterized the upper atmosphere's water distribution, reporting water vapor abundances for the first time at altitudes as high as $\sim 100-120$ km (Belyaev et al., 2021; Brines et al., 2024).

Here, we present the largest NOMAD water vapor data set measured with the Solar Occultation channel (SO) studied up to date. Building upon our previous water vapor retrievals mainly focused on the perihelion season (Brines et al., 2023, 2024), we extended the analysis to the aphelion season providing a complete view of the Martian water cycle throughout 3 complete Martian years. We have also improved our water vapor retrieval scheme in several directions as detailed below. We analyzed almost six years of NOMAD observations from April 2018 to December 2023, ranging from $L_S = 160°$ of MY 34 to $L_S = 160°$ of MY 37. As a first part of two-part series of papers, this data set allowed us to explore the seasonal and latitudinal variability of water vapor for three full MYs, revealing distinct patterns that repeat every year in addition to features observed only during specific years. Although a solar occultation experiment is not ideal for local time studies, we show below how the TGO orbit permits local time analysis at some latitudes and seasons. The high sensitivity of the NOMAD instrument allowed us to obtain water vapor abundances from $\sim 5-10$ km up to $\sim 110-120$ km altitude. In addition, and being the main topic of the second part of this paper, the extensive data set used in this work permitted a robust comparison between other NOMAD and ACS results and, for the first time, the application of cluster analysis techniques to Martian water vapor vertical profiles.

The structure of this paper is as follows: In Section 2 we describe the details about the NOMAD instrument and the data analysis. The results and discussion about the seasonal and latitudinal variability of water vapor profiles are presented in Sections 3 and 4 respectively. An analysis on the water vapor local time and longitudinal variability is presented in 5. Finally, a brief discussion about implications of this work on atmospheric escape processes is presented in Section 6. Section 7 summarizes the results, highlighting the main conclusions of this work. The comparison with NOMAD and ACS along with the cluster analysis will be presented in a future second part of this paper.

2. Data Set and Analysis

2.1. The NOMAD Instrument

The NOMAD instrument is a suit of three spectrometers able to sample the Martian atmosphere in different viewing geometries and at different spectral ranges operating between 0.2 and 4.3 μm covering the UV, visible and infrared (IR) regions of the spectrum (Vandaele et al., 2018). Those spectrometers are (a) the SO channel dedicated for solar occultation measurements in the IR (2.3–4.3 μm), (b) the Limb Nadir and solar Occultation covering a slightly smaller spectral range than SO (2.3–3.8 μm) but, in contrast, able to sound the atmosphere at nadir and limb geometries, and (c) the Ultraviolet and Visible Spectrometer sampling the spectral region between 200 and 650 nm and also very versatile regarding observational geometries.

Focusing on the SO channel, its design is based upon the Solar Occultation in the Infrared instrument onboard Venus Express (Bertaux et al., 2007). It uses an Echelle grating in Littrow configuration (the incident and reflected angles are equal) allowing for a spectral resolution of about $\lambda/\Delta\lambda \sim 17000$ (Neefs et al., 2015). During a typical solar occultation, NOMAD is able to sample the atmosphere every second, acquiring sets of spectra at about 1 km tangent height step. An Acousto Optical Tunable Filter (AOTF) in the optical path of the instrument is used to select up to six diffraction orders, which are measured quasi-simultaneously at every altitude. This feature is particularly useful to sample different spectral regions at different altitude ranges. By selecting proper combinations of orders, we are able to avoid optically thick spectral lines or to combine different target species, allowing flexibility and making the NOMAD instrument an excellent asset to build vertical profiles of diverse science contents with an unprecedented vertical resolution. An extended description of the NOMAD instrument was presented by Neefs et al. (2015) and the most recent instrumental characterization, in which Instituto de Astrofísica de Andalucia (IAA-CSIC) participated actively, is summarized in G. L. Villanueva et al. (2022) where major updates with respect to the early in-flight calibrations (Liuzzi et al., 2019; Thomas et al., 2022) were done, particularly in the AOTF and instrumental line shape (ILS) characterization.

The first of these, the AOTF, is best described by an asymmetric sinc-squared function with order-dependent parameters. The main issue of these kind of instruments is that the flux coming from adjacent orders propagates to the central target order. In the end, the flux measured by the detector resulted to be a combination of the main diffraction order plus an undetermined number of adjacent orders. The second key parameter, the ILS, was found to be a double Gaussian function whose widths and separation vary through each diffraction order. The AOTF and ILS parameters used in this work are those provided by G. L. Villanueva et al. (2022), assuming that the observed radiance contains flux from the central and the first four adjacent diffraction orders.

The latest characterization of the NOMAD SO channel are incorporated into our team's pre-processing and retrieval suite, a set of codes devoted to clean and invert the Level 1 calibrated transmittances supplied by the NOMAD PI team. These steps are under continuous revision and improvement, and are described in the following Section.

2.2. Data Analysis

The data processing and analysis performed at IAA-CSIC with NOMAD SO measurements have been extensively described in previous works (Brines et al., 2023, 2024; López-Valverde et al., 2023). In addition, at IAA-CSIC we follow a sequential inversion pipeline where other species such as CO (Modak et al., 2023), aerosols (Stolzenbach et al., 2023) and temperature and densities (López-Valverde et al., 2023) are also retrieved using NOMAD SO spectra.

For this work we used Level 1 calibrated transmittances (Trompet et al., 2023) from the latest pipeline processing at the Belgian Institute for Space Aeronomy and available at (ESA, 2024b). This data, however, contains some residual systematics due to instrumental effects such as bending on the spectra and spectral shifts which need to be addressed before retrieving the vertical profiles. With that goal, at IAA-CSIC we have developed a variety of pre-processing tools designed to identify and correct for the major systematics still present in the data. In particular, two of them are: (a) the bending of the spectral continuum (baseline) and (b) the spectral shift.

The residual bending, which varies from scan to scan, sometimes present variations of the transmittance through the diffraction order at a single altitude of up to ∼0.1. This large oscillation is not caused by dust or water ice particles or by molecular absorption bands but by variations on the temperature of the detector during the start-end of each atmospheric scan. In order to characterize its spectral shape and following a similar approach to those presented in other works analyzing NOMAD SO data (Aoki et al., 2019), we used a fourth order polynomial to fit the baseline of each spectrum. This is a common assumption by all teams working with NOMAD SO data. However, this removal needs to be done carefully since the presence of absorption lines may introduce a bias during the baseline characterization. For a precise removal, we used line-by-line forward model calculations carried out with the Karlsruhe Optimized Radiative transfer Algorithm (KOPRA, (Stiller, 2000)). This forward model has been adapted for the Martian atmosphere and more recently, updated with the NOMAD SO instrument characterization (AOTF and ILS) mentioned above. During the bending correction, the spectral shift is characterized simultaneously and eventually also corrected. The cleaning of the NOMAD SO data has been extensively described in López-Valverde et al. (2023) and Brines et al. (2023). The advantage of our methodology is that when using the KOPRA simulations we are taking into account any instrumental effects introduced into the spectra. These cautions are especially relevant for the analysis at high altitudes, where a poor characterization of the continuum can lead to large biases affecting the line depths, or for other purposes like the binning of spectra at different altitudes.

In addition to the cleaning, our pre-processing pipeline also provides an in-house characterization of the random component of the measurement noise using covariance matrices (C-matrix). Those matrices were computed for each solar occultation using dozens of spectra from the Top of the Atmosphere, with their diagonals containing the random oscillations in the measurements (C-noise). This C-noise resulted to be about 2–4 times smaller than the nominal measurement noise provided by (Thomas et al., 2022) at high altitudes. The largest component of this nominal value is a systematic spectrally correlated component that can be addressed during the inversion. Hence, using a much smaller random noise allowed us to improve the sensitivity of our inversions at the uppermost atmosphere (Brines et al., 2024).

Here we applied the IAA-CSIC processing pipeline to an extended NOMAD SO data set for water vapor, as an improved follow-up study of the work presented by Brines et al. (2023, 2024). We selected a total of 7,624 occultations taken during MY 34, 35, 36, and 37. These observations cover a Solar Longitude range from $L_S \sim 160°$ of MY 34 to $L_S \sim 160°$ of MY 37, being the most extensive NOMAD SO data set up to date. In Figure 1 we show the seasonal-latitudinal distribution of all the occultations indicating the morning observations from 1 to 11 a.m. (blue) and evening observations (red) from 1 p.m. to 11 p.m.

We analyzed all the NOMAD data available in four different diffraction orders: 134 (3,011–3,035 cm^{-1}), 136 (3,056–3,081 cm^{-1}), 168 (3,775–3,805 cm^{-1}) and 169 (3,798–3,828 cm^{-1}). The first two contain relatively weak absorption lines ($S \sim 10^{-21}$ cm^{-1}/(molecule·cm^{-2})), whereas the others show much stronger lines from the spectral region close to the ν_3 fundamental band which saturate at low altitudes (optical depth > 1). Since the AOTF allows for simultaneous measurement of different diffraction orders at each tangent height, for each occultation we can select the most convenient order at every altitude. This way we developed a strategy to combine up to four different pairs of orders, 134 or 136 with 168 or 169, using them at different altitude ranges. This methodology is possible only when both orders have been measured during the same solar occultation, and

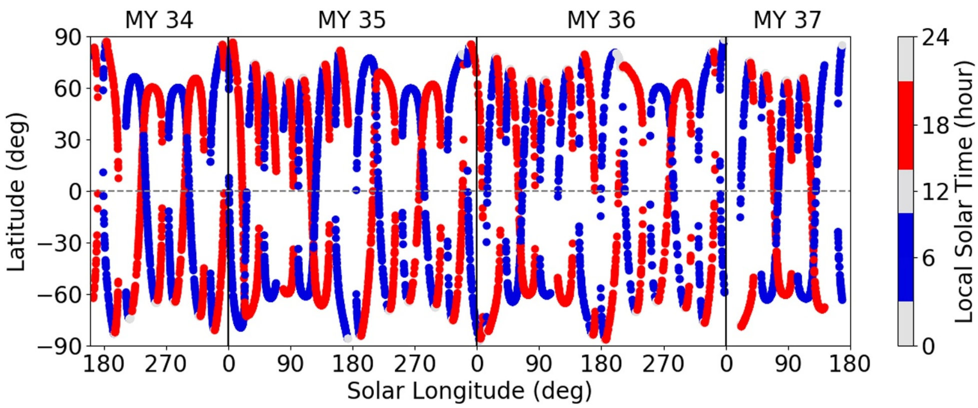

Figure 1. Latitude of the analyzed Nadir and Occultation for MArs Discovery Solar Occultation channel observations over solar longitude for mars years 34, 35, 36, and 37. Color indicates local solar time of the measurements, blue and red for morning and evening observations respectively. Vertical black lines indicate the beginning of each Martian Year.

although it limits the number of occultations available, it is necessary in order to obtain reliable vertical profiles from the bottom to the top of the atmosphere. Typically, we used low altitude orders (134/136) below 60 km and high altitude orders (168/169) above 60 km. This transition altitude, however, is not fixed. We used KOPRA simulations to calculate the curve of growth (variation of the line equivalent width with number of absorbents) of the strongest lines in orders 168 and 169 to estimate the water vapor partial pressure where those lines became optically thick. Then, using a first, approximate estimation of the water vapor volume mixing ratio (VMR) for each scan obtained during the pre-processing (based on the linedepth of the KOPRA simulations used during the bending and shift correction), we determined the optimal transition altitude for each occultation.

The water vapor profiles were obtained using the Retrieval Control Program (Clarmann et al., 2003), a multi-parameter non-linear least squares fitting of measured and modeled spectra, which incorporates KOPRA as its Forward Model. We followed the same methodology from our previous works (Brines et al., 2023), although with the improvements previously described in the measurement noise characterization and modifying the retrieval setup to permit the combination of orders, conducting a single global fit to data from two different diffraction orders. These improvements allowed us to obtain consistent vertical profiles for an extended vertical range from ~5 to ~120 km altitude. The lowermost altitude limit is due to the presence of aerosols, mostly suspended dust in the lower atmosphere, and varies depending on the season and location of the occultation. This bottom altitude for the inversion was determined during the pre-processing using an estimation of the slant opacity, cutting those altitudes with values of total optical depth along the line of sight larger than 2.0 (~0.1 in transmittance) and avoiding steep gradients larger than 0.08 km^{-1}. On the other hand, the upper altitude layer for the inversion is also variable with season and location and was set during the inversion using the averaging kernels computed during the retrieval. As done by Brines et al. (2023), here we also filter low values of averaging kernels, that is, we exclude some retrievals with low information content, typically with too weak absorption lines (below measurement noise), in order to avoid water abundances biased toward the a priori/climatology. During the inversions, for the a priori atmosphere we used pressure and temperature profiles extracted from specific runs of the Mars Planetary Climate Model (Mars-PCM, (Forget et al., 1999)) at the exact time and location of each solar occultation. The Mars-PCM runs were performed taking into account the best estimate of the dust optical depths from Montabone et al. (2020) for each MY, including the GDS in MY 34. Due to the lack of measured data, for MY 37 we used the same dust climatology than for MY 36. Since only the aphelion season of MY 37($L_S < 160°$) is analyzed here, corresponding to a period of low dust activity, we expect this climatology and Mars-PCM simulation to have a negligible impact on our results. In this regard, we recall that our inversions are highly independent on the assumed thermal structure. We used a first order Tikhonov regularization optimized for each diffraction order, first determined by performing synthetic retrievals and then fine tuned with a subset of actual inversions, which allowed us to select a regularization as a trade off between error propagation, vertical resolution and convergence rate.

Besides the propagation of the uncertainty in the measured transmittance during the inversion, we need to take into account and quantify other sources of errors: (a) the uncertainty in the reference atmosphere and (b)

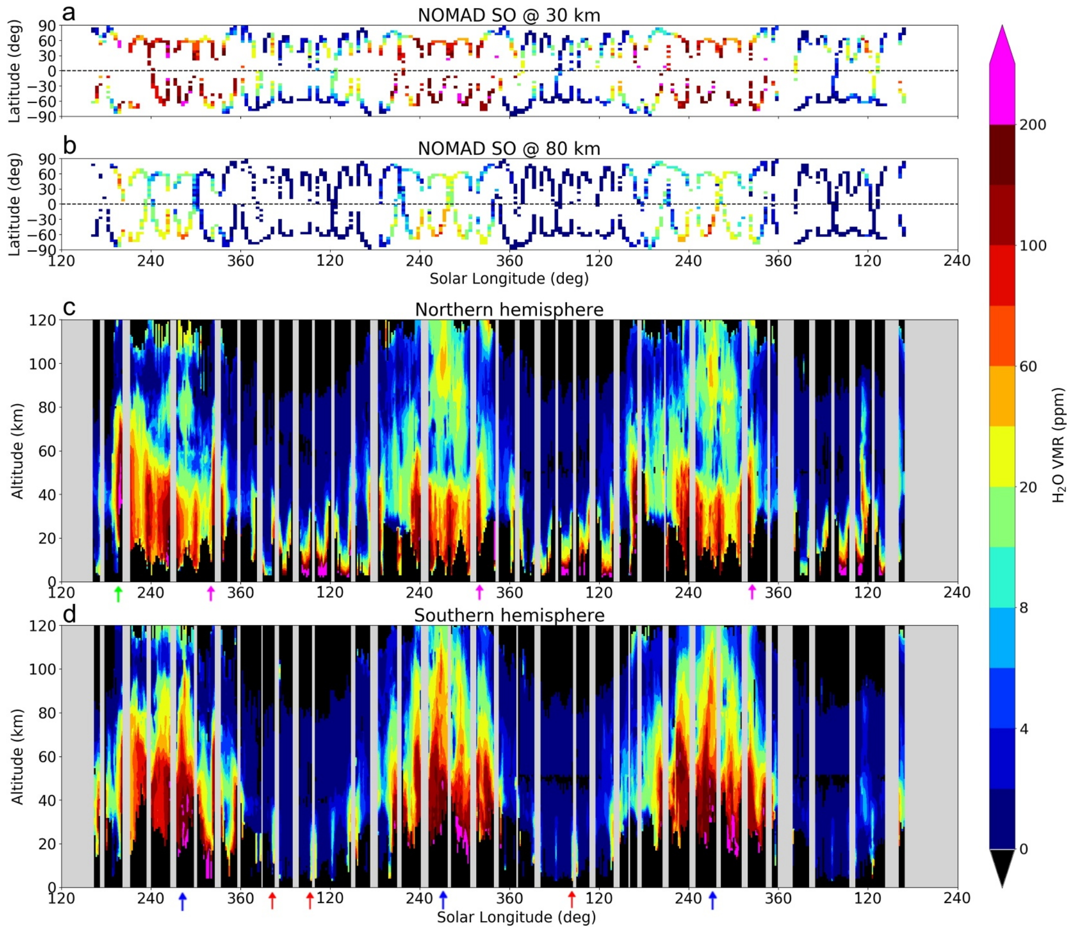

Figure 2. Vertical distribution of water vapor volume mixing ratio (VMR) over solar longitude during mars years 34, 35, 36, and 37 for the Northern (c) and Southern (d) hemispheres. Notice that the water vapor abundance's color scale is not linear. Top panel indicates the Latitude and H_2O VMR at 30 (a) and 80 (b) km altitude. Color arrows in the x axis indicate specific climatological features (see text for details).

uncertainty in the NOMAD instrumental calibration. We performed several sensitivity tests introducing modification on the a priori atmosphere, varying the temperature by ±5 K (estimated accuracy of our dedicated runs of the Mars-PCM) and introducing wave functions to simulate extreme ±10% oscillations in the pressure. These tests gave an uncertainty in the retrieved water vapor volume mixing ratio (VMR) of about 5%. Regarding the instrumental calibration, the major uncertainty comes from the AOTF characterization. We performed retrievals varying the AOTF parameters by 1σ, which resulted in impacts of about ±10% in the retrieved water vapor VMR. These uncertainties have to be taken into account when analyzing the results and during the comparisons with other teams.

Our processing and inversion scheme allowed us to successfully retrieve a total of 7,558 water vapor vertical profiles, which are analyzed next.

3. Seasonal Variability

The results of our retrievals, applied to the database mentioned in the previous section, are presented in Figure 2 and can be found in the public data repository (Brines, 2025). Water vapor VMR cross-sections at 30 and 80 km altitude are shown in Figures 2a and 2b respectively. The vertical variation of the water vapor profiles during all the analyzed MYs are shown in Figures 2c and 2d for the northern and southern hemispheres respectively. For visualization purposes in Figures 2a and 2b, we averaged the water vapor VMR measured within ±5 km altitude windows and within boxes of 5° in latitude and 5° in solar longitude. In Figures 2c and 2d we performed a weighted average of the profiles within bins of 1° in solar longitude. The latitude where each solar occultation was performed shown in the top panels exhibits a relatively quick variation from low to high latitudes (and vice versa). This peculiarity of the TGO orbit makes these maps difficult to analyze due to the fact that season, latitude and local time are linked, that is, changing simultaneously. Nevertheless, this representation allows for the identification of several climatological patterns, repeated year after year, and it allows to highlight specific distinct events. Hereafter, and for the benefit of the reader, we will use the notation L_S^X when referring to the solar longitude of the MY X.

3.1. Northern Hemisphere

When looking at the Northern hemisphere we observe that water vapor is more abundant at two altitude ranges depending on the season. During the perihelion season of each MY $\left(L_S \sim 180°-360°\right)$, water vapor presents large abundances (above 60 ppm) from about 10 km or below, up to 60 km. In particular, during $L_S^{34} \sim 190°-210°$ we observe a distinct enhancement of the water abundance of about 60–80 ppm at 70 km, reaching up to ∼20 ppm at 80 km. The ultimate source of this feature (indicated with a green arrow in the x axis in Figure 2c) during MY 34 was the GDS, and this abundance is not observed again with such intensity above 60 km in the northern hemisphere during the rest of the data set. The large dust abundance present in the atmosphere during that period lead to an increase of the temperature in the 40–60 km altitude range (Neary et al., 2020) which prevented the condensation of water vapor at those altitudes. As a consequence, water was able to be present in form of vapor at higher altitudes than usual. This topic was extensively discussed by previous works analyzing NOMAD data such as Aoki et al. (2019); Brines et al. (2023) and also by other TGO instruments like ACS NIR (Fedorova et al., 2020).

At the end of each Martian year, a regional dust storm, known as C-storm (Kass et al., 2016), usually occurs. So far, for MYs 34 to 36 those storms occurred at $L_S^{34} \sim 330°$, $L_S^{35} \sim 318°$ and $L_S^{36} \sim 314°$ with typical dust extinctions ranging from 0.0014 to 0.0020 km^{-1} (Martín-Rubio et al., 2024). In this type of storms, the top-most altitude were dust was observed was about 60 km in the southern hemisphere with maximum abundances of about 25 ppm at 40 km, in contrast to the ∼75 km top-most altitude and abundance peak of 70 ppm observed during the GDS (Liuzzi et al., 2020). Since these late-in-the-year dust events repeat every year, we cannot compare the water vapor response to it with a year without C-storm. Nevertheless, the seasonally decreasing water vapor abundances in the northern hemisphere during this period shows a reversed trend when the C-storms occur, with increased abundances below 60 km at $L_S^{34} \sim 330°$, $L_S^{35} \sim 320°$ and $L_S^{36} \sim 330°$ (indicated with pink arrows in the x axis in Figure 2c).

During the perihelion, the top most altitude where water is detected is ∼120 km, which corresponds with the highest altitude available by the current NOMAD calibration pipeline. Without any observational data available, any information obtained from above 120 km comes only from the a priori climatology used during the retrieval process. For that reason we limited our analysis to this altitude.

On the other hand, during the aphelion season $\left(L_S \sim 0°-180°\right)$ large water vapor abundances (above 60 ppm) seem to be more confined to low altitudes, from 5 to 10 km, showing a sharp decrease at 20–30 km. In addition, the uppermost tangent altitude where we can detect water vapor falls from about 120 km during perihelion to about 80 km during this period. This period corresponds to the northern summer, so the large abundance observed in the lower atmosphere corresponds to the well-known summer season's water release from the sublimation of the northern polar cap due to the increase of the temperature in this hemisphere (G. L. Villanueva et al., 2022).

3.2. Southern Hemisphere

The Southern hemisphere also shows distinct climatological patterns. Water is present in larger abundance and in a more extended vertical range during the perihelion season, coinciding with the southern spring and summer. During this period, also known as the "dusty season", local/regional dust storm events are frequent and the abundance of aerosols (dust) in the atmosphere is significantly larger than during other seasons. Due to its orbital eccentricity, Mars receives an enhanced solar flux at perihelion leading to a warmer southern summer (Smith et al., 2017) and an intense single cell meridional circulation, transporting species like water vapor from the south to the north. This effect is also affected by the topographic asymmetry between hemispheres, where the higher southern surface elevation results in a more intense thermal forcing of the mean circulation (Barnes et al., 2017).

Close to the summer solstice, around $L_S \sim 270°$ a strong injection of water vapor to the mesopause ($\sim$100 km) is repeated every year.

This feature, observed at high southern latitudes and marked with blue arrows in Figure 2d, has been discussed in a number of recent works using TGO observations (Aoki et al., 2022; Belyaev et al., 2021; Brines et al., 2024; Fedorova et al., 2021; G. L. Villanueva et al., 2022). Modeling efforts by Shaposhnikov et al. (2019) suggest that the vertical transport by the meridional circulation combined with the solar tides might be responsible of this strong water vapor pumping. We believe more modeling efforts, combined with the detailed data sets presented here, are still needed for a better description and understanding. This strong vertical transport, together with global dust storms seems to be an important mechanism for the effective injection of water vapor to thermospheric altitudes (above 100 km) affecting the thermal escape of hydrogen on Mars.

The southern autumn and winter seasons $\left(L_S \sim 0°-180°\right)$ show a clear contrast compared to the local summer. During the aphelion season, above 70–80 km the water vapor abundance is extremely low, below our detection limits matching the behavior observed in the northern hemisphere. In this case, only bursts of abundances of about $\sim$50 ppm below 40 km are observed occasionally at $L_S \sim 30°$ and $L_S \sim 90°$, corresponding to a latitudinal effect rather than seasonal trends, since these observations were taken at latitudes below 30° (see Section 4). In Figure 2d, these features are indicated with red arrows in the horizontal axis.

4. Latitudinal Variability

Although the interhemispheric asymmetry is evident in Figure 2, the large seasonal variation complicates other studies, like detailed latitudinal analysis. Hence, another representation of the profiles with a careful selection of appropriate occultations is required.

Here we selected different subsets of observations taken during relatively small ranges of L_S $(\Delta L_S = 30°)$, which show a significant latitudinal sampling. For a given latitude, in order to avoid mixing observations made at different local times, we split the sets considering occultations from only one terminator (morning or evening). We present the vertical profiles within those L_S windows using latitude-altitude maps, assuming that the observed water vapor distribution is caused only by the latitudinal variability. These cautions are also needed in order to analyze effects of the local time variations, which are discussed in the next Section.

4.1. Aphelion Season

In Figures 3 and 4 we show the latitudinal distribution of water vapor for the aphelion season (from $L_S = 0°$ to $L_S = 180°$) at the morning and evening terminators respectively. Here, the vertical profiles were averaged in 5° latitude bins. Observations from MYs 35, 36, and 37 within the same L_S window were used to compute the latitudinal distribution for each panel.

During both the aphelion and the periods close to the equinoxes ($L_S = 0°$ and $L_S = 180°$), most of the water vapor is confined to altitudes below 40 km. Particularly noticeable at mid latitudes ($\sim 30°-40°$) in MYs 35 and 36 we observe abundances below 20 ppm above 40 km during the evenings as shown in Figures 4a1, 4a2, 4b1, and 4b2. In contrast, during mornings, in Figures 3a2, 3b1, and 3b2 this limit is observed at 20–30 km. During this period of the year, close to the northern spring equinox, all Martian years show a similar structure, mostly symmetric respect to the equator and with the larger water vapor abundances appearing between 30°S–30°N. The global meridional transport induces a polar warming in the middle atmosphere ($\sim$60 km) as the downward branch of the cross-equatorial circulation descends at high latitudes (McCleese et al., 2010; Medvedev & Hartogh, 2007). This effect occurs at both hemispheres since the warmest surface temperatures at the equator lead to a two-cell Hadley circulation with a low latitude upwelling branch (Smith et al., 2017) and a descent branch at high latitudes causing an adiabatic warming. These warmer polar temperatures were also reported by ACS (Belyaev et al., 2022; Fedorova et al., 2023) and could be responsible for the water vapor enhancement observed at $\sim$40 km in both hemispheres (30°– 60°), particularly evident in Figures 3a1, 4a1, and 4b1. At these high latitudes and below this layer, water vapor abundance drops and this seems to be associated to the formation of water ice clouds (Fedorova et al., 2023; Stolzenbach et al., 2023). The enhancement of water vapor abundance in the middle atmosphere at high latitudes is observed again during the period close to the northern autumn equinox, as shown in Figures 3a6 and 3b6 for the morning and in Figure 4a6 for the evening terminator, which coincides with warm layers at polar latitudes, also observed by ACS MIR (Belyaev et al., 2022) and ACS NIR data (Fedorova et al., 2023).

10.1029/2024JE008916

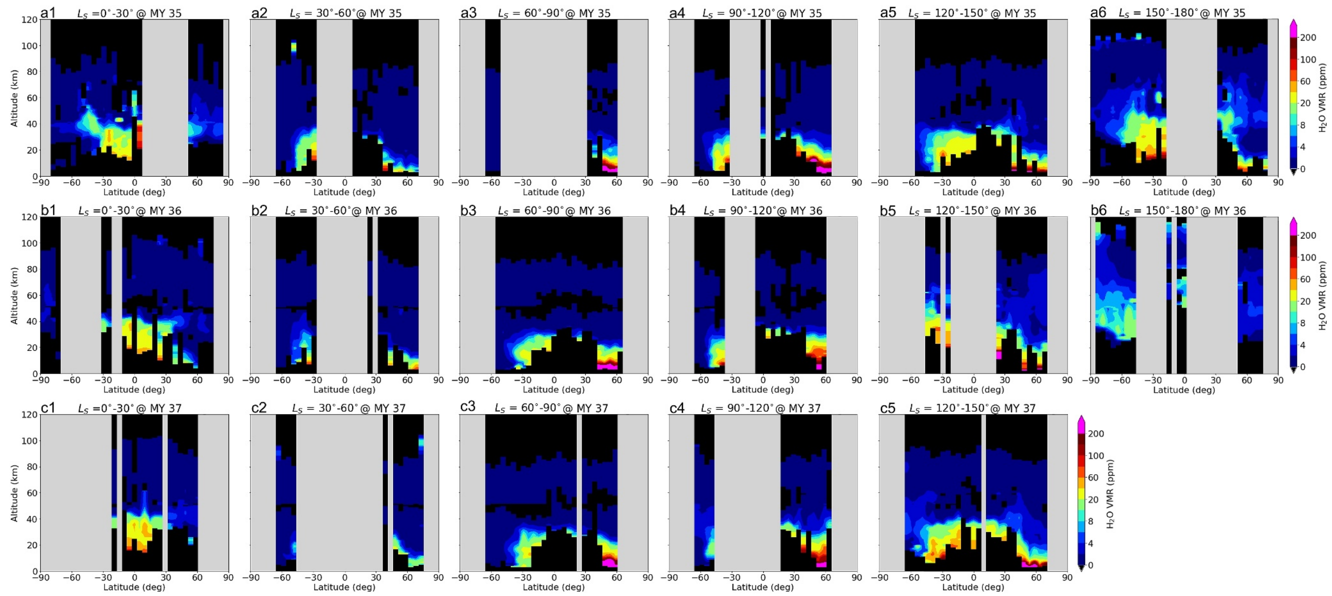

Figure 3. Latitudinal distribution of water vapor profiles during the aphelion season (from $L_S = 0°$ to $L_S = 180°$ of mars years 35 (top), 36 (middle) and 37 (bottom panels) from observations at the morning terminator. Each panel spans 30° in solar longitude.

Close to the northern summer solstice ($L_S = 90°$), the equatorial symmetric pattern previously described disappears, revealing an asymmetric structure between both hemispheres, very repetitive and similar during MYs 34, 35, and 36. As shown in Figures 3a3, 3a4, 3b3, 3b4, 3c3, and 3c4 for the morning and Figures 4a3, 4a4, 4b3, 4b4, 4c3, and 4c4 for the evening terminator, the distribution of water vapor is shifted toward the northern hemisphere. The increase of the temperatures at high northern latitudes leads to the sublimation of the polar cap in the summer hemisphere, releasing large amounts of water resulting in low altitude (below 10 km) VMRs >200 ppm at high latitudes ~60°N. These large abundances in the northern hemisphere are more confined to lower altitudes during the mornings than during the evenings, possibly due to the temperature differences in the lower atmosphere (of about 5–10 K colder morning temperatures during this season (Fedorova et al., 2023)) and to the formation of nighttime ice clouds. Precipitation of water ice crystals from these ice clouds at nighttime and their subsequent

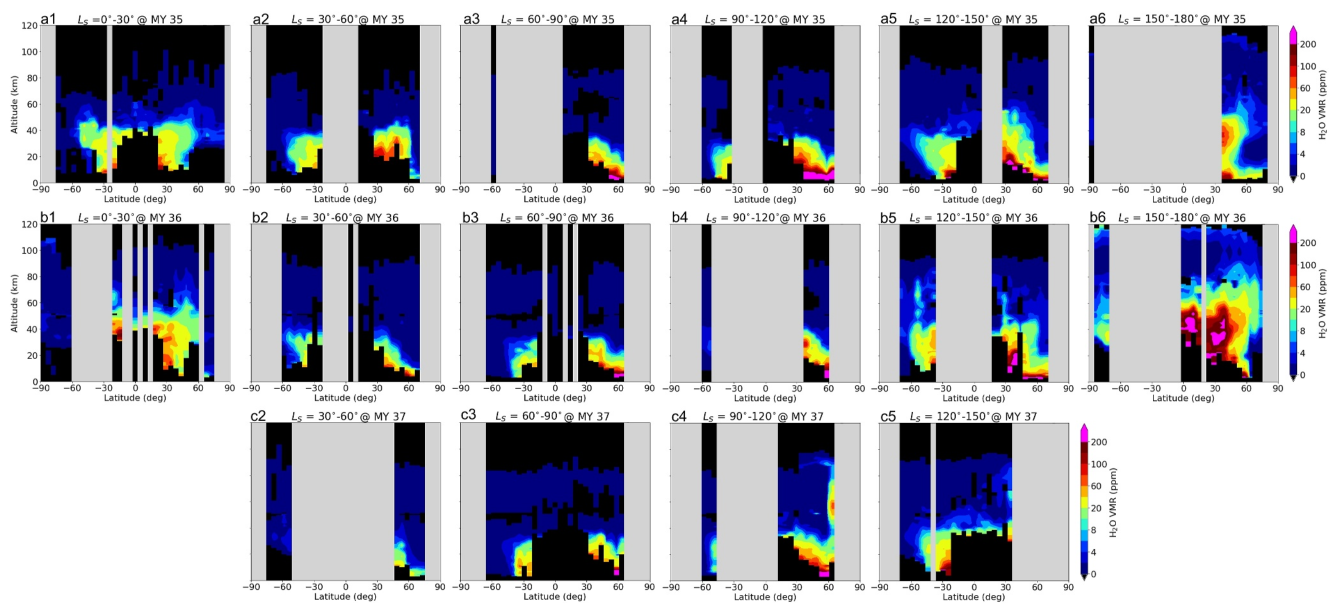

Figure 4. Same as Figure 3 but for evening terminator observations.

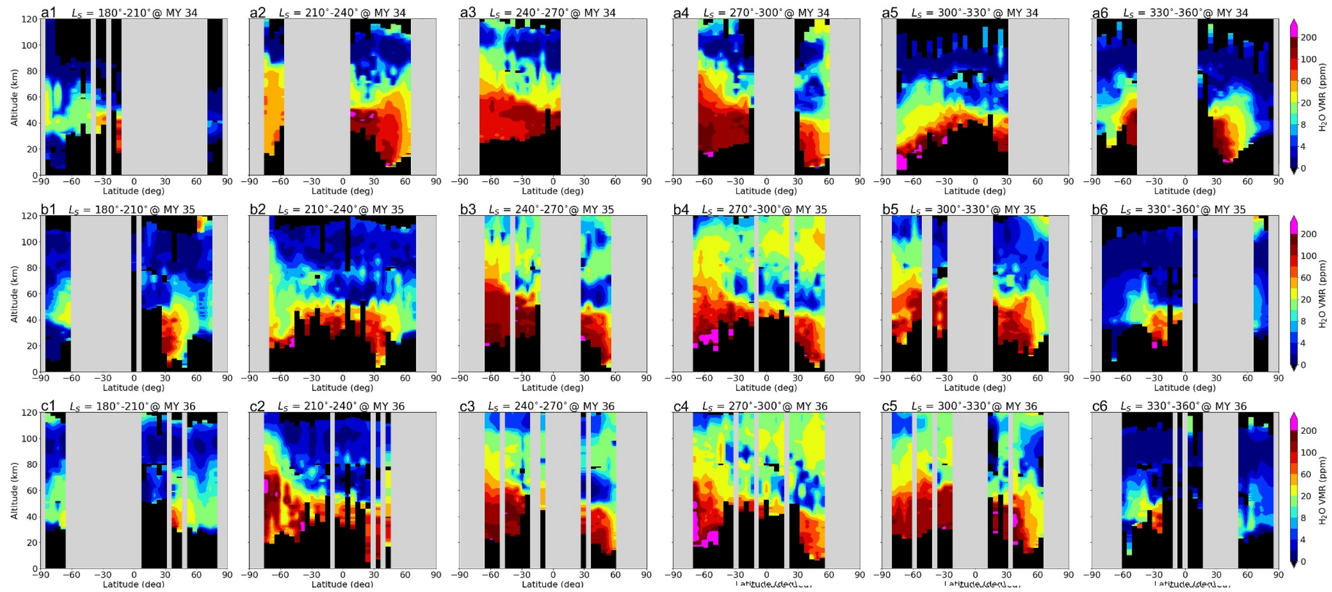

Figure 5. Latitudinal distribution of water vapor profiles during the perihelion season from $L_S = 180°$ to $L_S = 360°$ of mars years 34 (top), 35 (middle), and 36 (bottom panels) from observations at the morning terminator. Each panel spans 30° in solar longitude.

sublimation during the morning, could lead to water vapor being closer to the surface after sunrise (Daerden et al., 2010).

At the end of this first half of the year, close to the northern autumn equinox, the vertical extent of the observed water vapor abundances are significantly larger than during the spring equinox, specifically during evenings (Figure 4b6), where VMRs >100 ppm are present at ∼50 km altitude in the northern hemisphere. Evening temperatures observed by ACS were larger during this period than during the northern spring equinox (Belyaev et al., 2022), possibly increasing the altitude where water ice clouds form. This is also suggested by Aoki et al. (2022) based on GEM-Mars simulations, who found this late aphelion water vapor enhancement in the northern hemisphere related to a lower rate of cloud formation during daytime.

It is worth mentioning a noticeable water vapor enhancement observed only in MY 37 at ∼60°N during $L_S \sim 110°$, as shown in Figure 4c4. This kind of enhancements, showing abundances as large as 50 ppm reaching altitudes of about 60 km are rarely observed during this season at this high northern latitudes. In a preliminary analysis of this feature we have discarded it to be a bias in our retrievals, and currently ongoing work indicates that this water vapor injection to high altitudes could be related with an out-of-season dust event triggering an unprecedented water pumping. We are currently investigating this particular phenomenon and a dedicated study will be published in the future.

4.2. Perihelion Season

In Figures 5 and 6 we show the latitudinal distribution of water vapor during the perihelion season (from $L_S = 180°$ to $L_S = 360°$) of MYs 34, 35, and 36 at the morning and evening terminators respectively. Similarly to what is shown for the aphelion season, profiles were averaged in bins of 5° latitude.

First, in Figures 5a1, 5b1, 5a1, 6a1, 6b1, and 6c1, hints of the typical equinoctial symmetric structure are visible, being significantly more intense than its aphelion analog. During this period $\left(L_S^{34} = 180°-210°\right)$, MY 34's GDS reached its peak and its effects are noticeable when comparing Figure 6a1 with the same period of MYs 35 and 36 (Figures 6b1 and 6c1 respectively). The GDS reached its mature phase at $L_S^{34} = 198°$ and the peak on the temperature increase due to the large dust abundance was registered around $L_S^{34} = 207°$ (Kass et al., 2020). During this period, the effects of the storm can only be observed at the evening terminator due to the sampling location and timing of NOMAD measurements, capturing the GDS during the evenings. Nevertheless, the interannual variability between MY 34 and the following years is evident. As shown in Figure 6a1, in MY 34 we observe water abundance of about 100 ppm even at 70–80 km altitude in the southern hemisphere at ∼60°

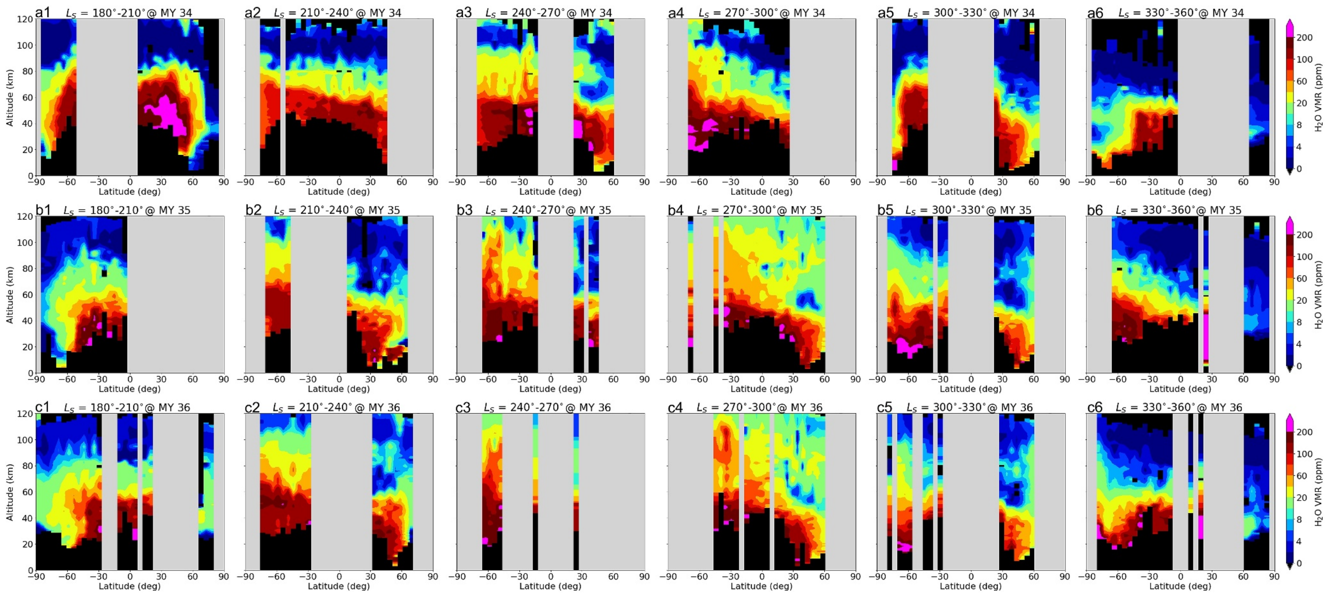

Figure 6. Same as Figure 5 but for evening terminator observations.

latitude, showing a sharp decrease toward polar latitudes at >80°S. In the northern hemisphere, the distribution is similar, with large abundance of about 200 ppm below 40 km and again, a sharp decrease at >65°N. The larger abundances at high southern latitudes are possibly due to the weakening of the Southern Polar Vortex induced by the storm (Streeter et al., 2021). During non-GDS years the abundance at latitudes >60°S was not larger than 20 ppm as shown in Figures 6b1 and 6c1.

After the GDS, during its decay phase at $L_S^{34} = 213-230°$ (Kass et al., 2020), the interannual variability is more noticeable in the northern hemisphere. In Figures 5a2 and 6a2, for both terminators morning and evening terminators respectively, at latitudes 0°N–30°N we observe water abundance of about 100 ppm at 50 km during MY 34, whereas in the following years this values are observed only below 20–30 km (Figures 5b2, 5c2, 6b2, and 6c2). In contrast, in the southern hemisphere at latitudes >60°S we notice larger abundances below 60 km at the evening terminator during the years without GDS, with at least 100 ppm. These differences between years with and without global dust storms were reported by Brines et al. (2024), and Pankine et al. (2023) found systematically lower water vapor abundance at high southern latitudes during the years with storms compared to the years with regular dust activity.

For the following sets between $L_S = 240°-300°$ the distribution and abundance of water below 60 km is similar in all the three MYs, although MY 34 shows lower abundances particularly during morning observations, as shown in Figures 5a3, 5b3, and 5c3, feature already reported by Brines et al. (2024).

In Figures 5a3, 5a4, 5b3, 5b4, 5c3, and 5c4 for the morning, and Figures 6a3, 6a4, 6b3, 6b4, 6c3, and 6c4 for the evening terminator, we observe an asymmetric pattern with more vertically extended abundance in the southern hemisphere and repeated systematically every year. This is possibly due as a result of the vertical transport produced by the upwelling branch of the Hadley cell, which intensifies during southern summer due to the enhancement of the solar flux produced by the orbital eccentricity of Mars and also to the north-south topography dichotomy (Richardson & Wilson, 2002). Above 60 km, however, some interannual differences arise. MYs 35 and 36 present a large injection of water vapor to the upper atmosphere particularly intense at the evening terminator and only at mid-high southern latitudes, the larger enhancement being located at 50°S–60°S. We observe abundances of about 50 ppm up to 100 km as shown in Figures 6b3 and 6c3, feature which appears later and with reduced intensity in MY 34 (Figure 6a4). This observed plume, reported by ACS (Belyaev et al., 2021) and NOMAD (Aoki et al., 2022; G. L. Villanueva et al., 2022), was recently deeply analyzed by Brines et al. (2024), who presented an extended discussion about the nature of this phenomena and suggested long term effects of the GDS to be responsible of its weak and delayed appearance during MY 34. During this same period ($L_S = 240°-300°$), at the northern hemisphere we observe a layer of low water vapor abundance below 20 ppm at 40–60 km. This depletion of water seems to be present at both terminators although is particularly noticeable at the morning terminator in Figure 5 and, where water increases again above the depletion, forming another layer of >20ppm visible at ∼100 km (Figures 5b4 and 5c4). On one hand, these layers of depleted water vapor coincide with regions where water ice clouds were observed by Fedorova et al. (2023). On the other hand, the presence of larger abundance above, as discussed in the following section, suggests either a more efficient northward transport through the meridional circulation at high altitudes during mornings than during evenings, or sublimation of the water ice clouds below due to the presence of a morning warm layer at ∼80 km (Fedorova et al., 2023).

As discussed in the previous section, the last part of the year is particularly interesting due to the frequent occurrence of C-Storms. These dust events warmed up the atmosphere and their effects allowing water vapor to reach higher altitudes can be observed more clearly at the evening terminator in Figures 6a5 and 6b5 for MYs 34 and 35 respectively. These years show larger water vapor abundance in a more extended vertical range (up to 60–70 km) at high southern latitudes (∼60°). These regions were sampled by NOMAD during most of the duration of the C-Storm in MY 34 and during the decay phase of the storm in My 35. Interestingly, the effects on the water vapor are not so evident at these high southern latitudes in MY 36 (Figure 6c5), with lower abundances at 40–60 km compared to previous years during the same period. The reason of this difference is mostly due to the NOMAD sampling. The C-Storm in MY 36 started at L_S ∼ 308° and lasted until L_S ∼ 320° (Martín-Rubio et al., 2024). During this period, unfortunately only few observations were available from NOMAD, most of them taken only at L_S 309° at mid latitudes and missing the peak and decay phase of this storm. This observational bias limits the characterization of the storm effects on water vapor during MY 36. Just 1° in solar longitude after the starting of this storm might not be enough to reveal relevant enhancements on the water vapor global circulation. Additionally, at the end of the year, the larger abundances observed in MY 34 (Figure 5a6) compared to the following ones (Figures 5b6 and 5c6) particularly in the morning terminator could also be attributed to effects of the C-Storm in MY 34. This year, unlike MYs 35 and 36, the storm triggered later in time and lasted for a longer period ranging from L_S 319° to L_S 340° (Martín-Rubio et al., 2024).

5. Local Time and Longitudinal Variability

The selection of the L_S ranges in Figures 3, 4, 5, and 6 was made in order to allow for the interannual comparison throughout different seasons. Although morning and evening terminators are clearly differentiated, not all latitudes and longitudes were sampled at both terminators for all the profile sets. For each TGO orbit, typically NOMAD measures a sunrise and a sunset at each hemisphere, thus making the analysis of local time variations complicated. Despite this limitation, the TGO orbital geometry allows for the sampling of nearby latitudes and longitudes at both terminators during a few L_S ranges throughout the Martian year. For this study we selected another subset of profiles in some L_S intervals not larger than 30° in order to minimize seasonal variability effects as much as possible. We selected a total four L_S windows, two for each hemisphere. The selection of these four L_S intervals is not arbitrary, but rather due to the fact that the measurements offer good longitudinal coverage. In order to allow for a comprehensive analysis of local time variations these sets of observations allow the comparison of similar latitudes and longitudes during the morning and evening terminators. The terminator is defined using a fixed Solar Zenith Angle SZA = 90°, but the local time along this region varies with the latitude. The most common local times of NOMAD SO observations are 6 a.m. and 6 p.m. for the morning and evening respectively. For this study we consider as morning (evening) observations all those measured at 6 a.m. ± 5 h (6 p.m. ± 5 h). With this restriction, the morning and evening sets are separated by at least 2 h during midday (midnight), and observations from 11 a.m. to 1 p.m. (11 p.m. to 1 a.m.) are excluded. The selected L_S windows are scattered through the year, covering the aphelion and perihelion seasons on both hemispheres. For each L_S window we obtained longitudinally averaged water vapor profiles from MYs 35 and 36 within longitude bins of 5° at each terminator. The distributions were obtained at latitudes between 55°–65° in each hemisphere, where the majority of the NOMAD observations are taken. In Figure 7 we show the longitude-altitude maps representative for the aphelion (four top panels) and perihelion (bottom four panels) seasons on the northern (left panels) and southern (right panels) hemispheres.

Longitudinal variations were reported as particularly relevant at tropospheric altitudes (Pankine, 2022; Smith, 2002). In order to assess this, for each longitudinal map we added a second panel showing the averaged water vapor profiles within regions of 90° in longitude. Despite some variability in the longitudinal distribution, larger during the second half of the year, for a given L_S, these 90° longitudinal averages show similar vertical

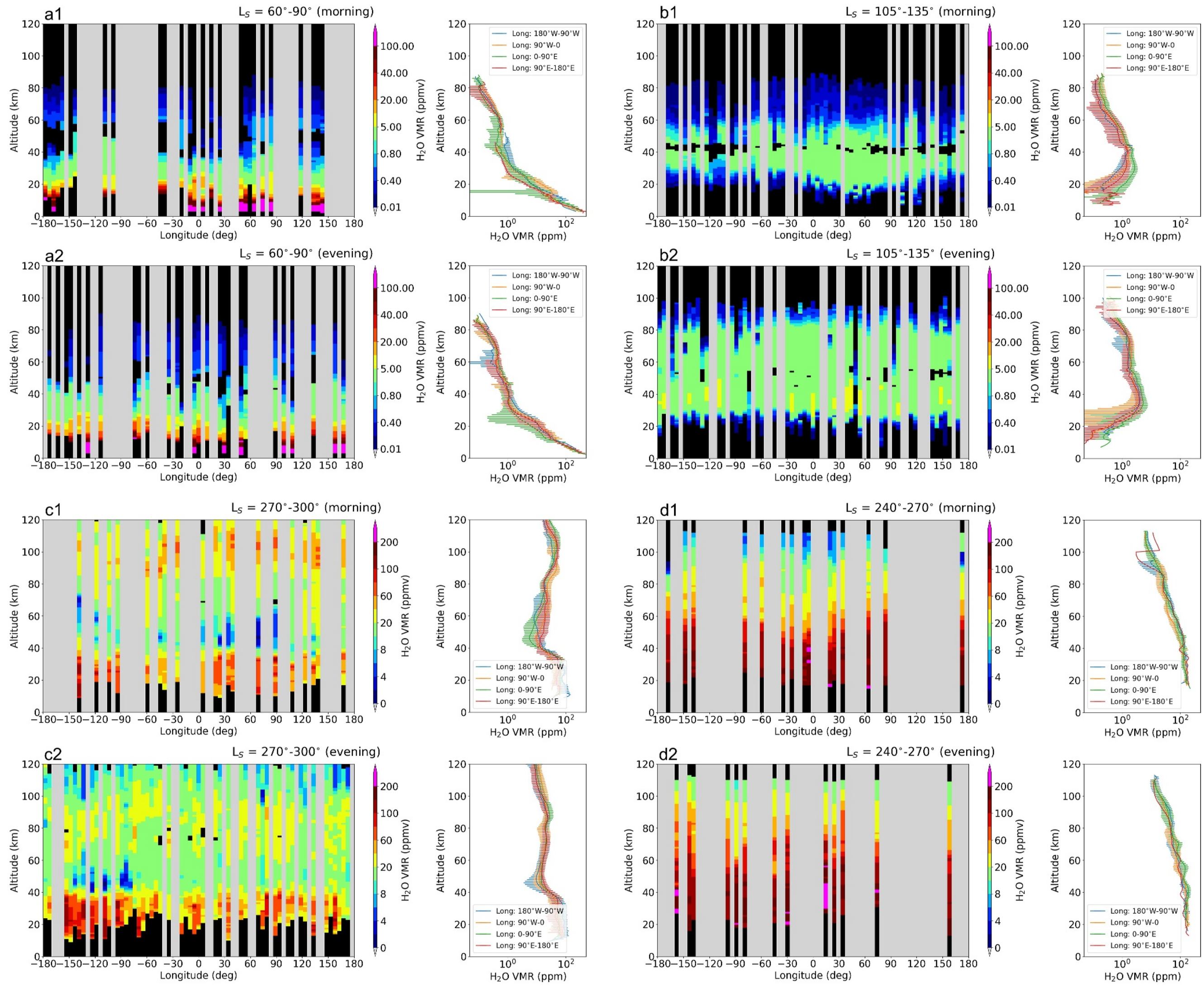

Figure 7. Multi-annual average of longitude-altitude distribution of Nadir and Occultation for MArs Discovery solar occultation channel water vapor volume mixing ratio at latitudes 55°–65° at the northern (left) and southern (right) hemispheres. (a1 and a2) Northern's hemisphere longitudinal distribution at $L_S = 60° - 90°$ during morning and evening respectively. (b1 and b2) Southern's hemisphere longitudinal distribution at $L_S = 105° - 135°$ during morning and evening respectively. (c1 and c2) Northern's hemisphere longitudinal distribution at $L_S = 270° - 300°$ during morning and evening respectively. (d1 and d2) Southern's hemisphere longitudinal distribution at $L_S = 240° - 270°$ during morning and evening respectively. For each longitudinal map, left panel shows averaged profiles at longitudes 180°W–90°W (blue), 90°W–0° (orange), 0°–90°E (green) and 90°E–180°E (red). Errorbars indicate the standard deviation within each longitude interval.

structures. The strong longitudinal variability discussed by Pankine (2022) and Smith (2002) apply for water vapor integrated columns, extremely sensitive to the very first few kilometers above the surface. Our retrieved profiles suggest a nearly homogeneous longitudinal water vapor distribution throughout the planet at latitudes 55°–65° in both hemispheres above 10–20 km, region that barely contributes to the estimation of the water vapor columns. In Figure 8 we show the ratio between morning and evening averaged profiles for each L_S window and 90° longitudinal bin from Figure 7.

Focusing first on the aphelion season, Figures 7a1 and 7a2 reveal a similar water vapor distribution in the northern hemisphere during both morning and evening above 40 km. Also, Figure 8a shows larger evening water vapor abundances about four to five times larger at ~30 km at some longitudes in the northern hemisphere. However, the largest differences between dawn and dusk water vapor profiles are observed in the southern hemisphere. Figure 7b1 shows a layer with the largest water vapor abundances of about 5 ppm at 30–50 km altitude during the morning. This homogeneous structure around the planet becomes thicker by the end of the day, ranging from 20

10.1029/2024JE008916

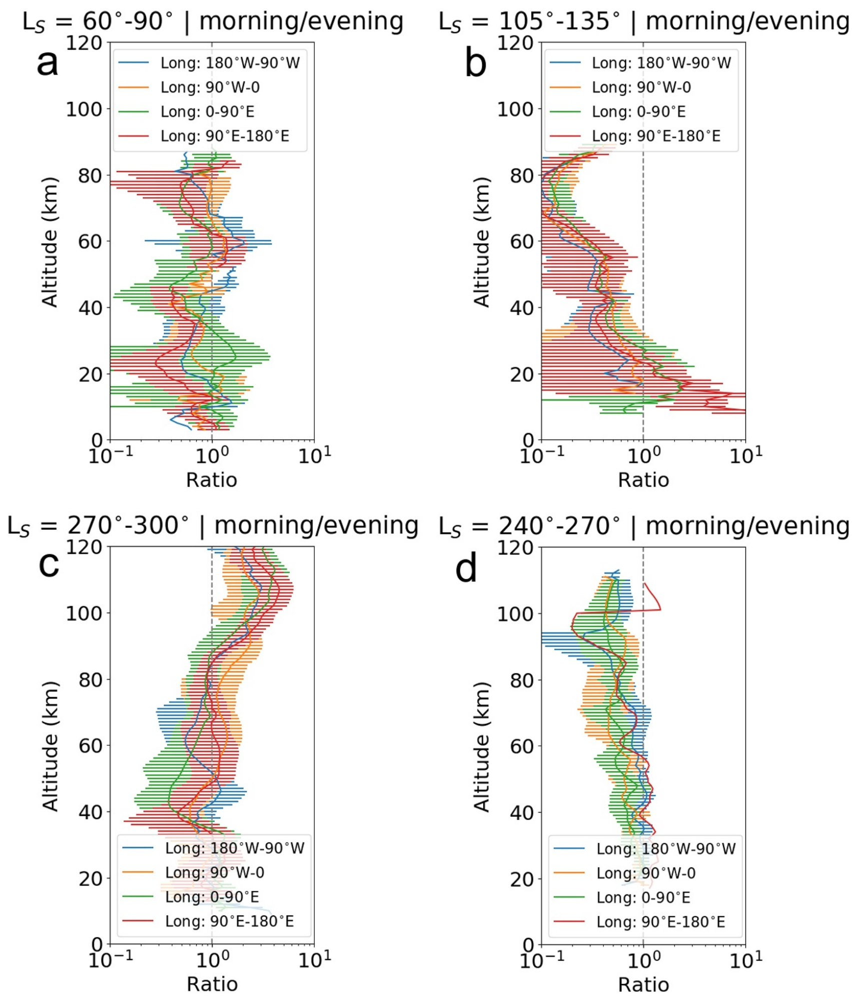

Figure 8. Vertical profiles showing the ratios morning/evening at (a) $L_S = 60° - 90°$, (b) $L_S = 105° - 135°$, (c) $L_S = 270° - 300°$ and (d) $L_S = 240° - 270°$. Left panels correspond to observations in the northern hemisphere whereas right panels correspond to observations in the southern hemisphere. For each panel, the color indicates the longitudinal range where the ratio was computed: 180°W−90°W (blue), 90°W−0° (orange), 0°−90°E (green) and 90°E−180°E (red). Errorbars indicate the uncertainty due to the variability within each longitude interval.

up to 80 km altitude during the evening as shown in Figure 7b2. This leads to more than 10 times larger abundances at 60–80 km during the evening than during the morning, as shown in Figure 8b. These diurnal differences could be driven by the colder temperatures in the southern hemisphere during nighttime, leading to a larger water condensation. This is supported by observations from the Compact Reconnaissance Imaging Spectrometer for Mars, that reported water ice clouds at mesospheric altitudes above 50 km during $L_S = 35° - 155°$ (Clancy et al., 2019). Additionally, Stcherbinine et al. (2022) shows the presence of water ice clouds observed with ACS-MIR at $L_S \sim 130°$ at mid southern latitudes and Mars Express VMC Images also reveals an intense activity in mesospheric cloud formation at twilights during $L_S = 90° - 180°$ at latitudes ∼50°S (Hernández-Bernal et al., 2021).

During the perihelion season, at 55°N–65°N, the largest longitudinal variations are observed at 40–70 km altitude as shown in Figures 7c1 and 7c2, for the morning and evening terminators respectively. This altitude region corresponds with a minimum in the water vapor abundance and correlates with the region with the lowest temperatures during this season and latitude (Fedorova et al., 2023). In addition, those low temperatures also show prominent longitudinal variations (Fedorova et al., 2023), which might be the reason of the observed variations in water vapor. Interestingly, at these altitudes the lowest water vapor abundances are observed at 150°W–120°W and 30°E–90°E during the morning but only at 150°W–90°W during the evening.

Journal of Geophysical Research: Planets 10.1029/2024JE008916

The contrast between morning and evening becomes more noticeable during this perihelion season than during the aphelion. Figure 8c shows that the water vapor abundances are similar at both terminators below 40 km. However, a clear evening enhancement can be seen at 40–80 km, particularly at the longitudes with the lowest water vapor abundances. Higher up, at ∼100 km the situation reverses revealing a morning enhancement systematically at almost every longitude within latitudes between 55°N and 65°N. A tentative explanation for the presence of this layer could be the following: Water ice clouds form after sunset and during nighttime (Smith, 2019) and are observed later in the morning at altitudes 60–80 km (Stcherbinine et al., 2022). This water ice cloud layer correlate with the depleted layer of water vapor observed in Figure 7c1. In the morning, the warm layer observed around 80–90 km (Fedorova et al., 2023) possibly sublimates the water ice clouds at those altitudes. This temperature inversion might prevent water vapor to immediately reach lower altitudes, confining the water vapor at high altitudes. Following this tentative explanation, during daytime, this warm layer descends in altitude (as shown in Fedorova et al., 2023) an therefore the water ice clouds will largely dissipate or move down to the 40–60 km layer in the evening. A more isothermal vertical structure allows a more homogeneous water vapor vertical distribution, as observed in Figure 7c2.

Besides this tidal variations in the thermal profile, we cannot discard additional processes like daytime photodissociation to play a role in this high altitude morning-evening difference. At this season (northern winter) water vapor in the northern hemisphere is supplied from the southern one via meridional transport, particularly strong during this season (Shaposhnikov et al., 2019). Water vapor photolysis column rate during $L_S \sim 270°$ is about 4-5 $\times$ 10^{10} cm^{-2} s^{-1} (Alday et al., 2021). This water vapor destruction rate has to be compared with the refilling by the global circulation at these high altitudes during both, daytime and nighttime. This is a complicated task and existing literature does not provide enough clues to estimate reliable water meridional fluxes at these latitudes, altitudes and season. For this reason, this numerical analysis should be performed more precisely with the help of a GCM. Additional work in this direction should be very beneficial to clarify this issue. For example, by quantifying the winds and stream functions predicted by data assimilation models feed with these exact NOMAD data (Holmes et al., 2021).

In the southern hemisphere, similar to the northern one, large water vapor longitudinal variability can be observed in Figures 7d1 and 7d2, for the morning and evening terminators respectively. Unfortunately, the lack of data at specific longitudes do not allow to draw solid conclusions. Nevertheless, at the morning terminator, the observed distribution seems to show larger vertical water vapor extent around 150°W–90°W and 150°E–90°E, with a minimum at 30°W–30°E. This longitudinal wave pattern is not clear during the evening. Nevertheless, besides these morning longitudinal variations, an overall local time variability can be observed. As illustrated in Figure 8d, averaging water vapor profiles in 90° bins reveals a systematic trend toward larger evening abundances. As we observe this in all the longitudinal bins, we conclude that diurnal variations are larger than the longitudinal variability.

6. Discussion

In this section we present a brief discussion about implications for atmospheric escape, one of the main planetary processes affecting the long-term evolution of the climate of Mars. The recent solar occultation observations of the Martian atmosphere with the ExoMars TGO mission permits a long waited systematic and detailed analysis of the atmospheric vertical structure. These kind of studies are essential to understand one of the main unknowns with respect to the Martian climate: the water loss. This escape mechanism is acting slowly but continuously on Mars since at least the last 4 billion years (G. Villanueva et al., 2015; G. L. Villanueva et al., 2021). This loss to space is controlled by the amount of water vapor that is able to reach high altitudes, and which after being photo dissociated, liberates the hydrogen that actually escapes (Chaffin et al., 2021). On this context, recent studies have tried to characterize the water vapor distribution above 100 km and its associated escape (Belyaev et al., 2021; Brines et al., 2024). These studies focused the analysis on the perihelion season and in the southern hemisphere where the larger temperatures and hence, the stronger vertical transport, are expected. The study and results presented in this work are intended to exploit the NOMAD solar occultation data and to contribute to the description of the water vertical profiles and its connection to the escape of hydrogen to space.

One of the most striking results this study is the potential contribution not only of the southern but also of the northern hemisphere to the water escape. The large water abundances observed at high altitudes and at high northern latitudes in the morning, if present during the whole day time period, could be extremely relevant for the total budget of hydrogen prone to escape to space. NOMAD and ACS instruments onboard TGO now permit the study of this upper regions of the atmosphere and systematically correlating water with temperature and aerosol observations will be essential for constraining the processes going on at these altitudes. Additionally, the unexpected water increase in the northern hemisphere during the aphelion of MY 37 reported here, might highlight the necessity to consider the contribution of the northern summer season to the hydrogen escape processes. This interesting event requires further analysis, not only with NOMAD observations, but also with additional limb observations from the Mars Climate Sounder, which can provide temperature and aerosols extinction (Clancy et al., 2012), and observations from the Emirates Mars Ultraviolet Spectrometer, onboard the Emirates Mars Mission, which can provide hydrogen density at the exobase (Holsclaw et al., 2021). Such cross-mission analysis will be performed and presented in future publications.

7. Summary and Conclusions

For the work presented here, we analyzed NOMAD SO spectra from more than 7,000 occultations collected over MYs 34 to 37, covering four diffraction orders and combining them to avoid extremely optically thick conditions (or saturated absorption lines). Our pre-processing pipeline significantly improved the correction of systematic errors in the NOMAD SO data compared to previous analyses (Brines et al., 2023), particularly for high-altitude measurements where accurate baseline characterization is crucial. This improvement enabled the consistent retrieval of extended water vapor vertical profiles ranging from approximately 5–120 km altitude during a single solar occultation.

In this study, we present the seasonal and latitudinal variability of water vapor in the Martian atmosphere as well as a detailed analysis of the water vapor local time variability. We provide the most extensive water vapor climatology to date based on NOMAD observations, showing strong seasonal variations in water vapor distribution on Mars. Distinct differences between perihelion and aphelion seasons in both hemispheres are evident, with the southern hemisphere experiencing larger and extended water vapor abundances during the southern summer. Our data reveals that these variations and interhemispheric asymmetry are influenced by factors such as dust storms, polar cap sublimation and Martian orbital eccentricity.

Particularly during equinoxes, water vapor is mostly confined to low altitudes and at latitudes lower than 60°–50°, showing abundances below 20 ppm above 30 km during the mornings and above 40 km during the evenings. However, the vertical extension of this water vapor layers and its peak abundances are larger during the northern autumn than during the spring equinox. The latitudinal distribution is symmetric with respect to the equator, repeatedly during all MYs. In addition, our observations reveal a 40 km altitude layer of abundances of about 20 ppm at ±60° latitude as a consequence of the polar warming effect.

The effects of injecting water vapor at high altitudes are visible during different periods of the MYs analyzed here. During the GDS after the northern autumn equinox during MY 34, we observe abundances of about 80 ppm at 70 km altitude. In the period corresponding to the decay phase of the storm, and at altitudes below 60 km, we observe larger abundances during MYs 35 and 36 than during MY 34. During the perihelion, all MYs show a similar asymmetric distribution, with larger and more vertically extended abundances at the southern hemisphere. However, MY 35 and 36 show a more intense vertical transport at 60°S, injecting abundances of about 50 ppm at 100 km altitude. Moreover, during this period, we observe hints of the presence of water ice clouds in the form of depletion layers of water vapor in the northern hemisphere between 40 and 60 km altitude, as well as larger abundances observed in the morning compared to those observed in the evening at 100 km. This morning enhancement correlates with a temperature inversion layer observed just below.

Finally, interestingly MY 37 shows intense upward transport in the northern hemisphere at $L_S \sim 112°$ which was not observed during other MYs and that seems to be related with a regional dust storm taking place during that same period.

All the results presented in this work extend and complement some of previous recent TGO studies on water vapor vertical profiles (Aoki et al., 2022; Belyaev et al., 2021; Brines et al., 2023, 2024), providing additional insight into morning/evening water vapor variability.

We have described in this work the major features observed in the water vapor distribution obtained. We believe these data set contain completely new insights into the vertical distribution of atmospheric water vapor on Mars, which shall foster future comparisons and shall permit validation of predictions by global climate models. A follow up work, presented as Part II, will be devoted to further studies of these NOMAD water vapor abundances, using cluster analysis techniques and with a focus on the comparison with vertical profiles from other data sets and with simulations with the Mars-PCM.

Data Availability Statement

The NOMAD SO Level 1a calibrated data used in this work are available at the European Space Agency Planetary Science Archive (ESA, 2024b). More information about the data on the PSA can be found in the NOMAD Experiment-to-Archive Interface Control Document (ESA, 2024a). The results retrieved from the NOMAD SO measurements presented in this work are being archived and available at Brines (2025). The data generated for this publication is also available through the VESPA portal at https://vespa.obspm.fr/planetary/data/ look for NOMAD/TGO.

Acknowledgments

The IAA-CSIC team acknowledges financial support from the Severo Ochoa grant CEX2021-001131-S and by grants PID2022-137579NB-I00 and PID2022-141216NB-I00 all funded by MCIN/AEI/10.13039/501100011033. A. Brines acknowledges financial support from the grant PRE2019-088355 funded by MCIN/AEI/10.13039/501100011033 and by 'ESF Investing in your future'. ExoMars is a space mission of the European Space Agency (ESA) and Roscosmos. The NOMAD experiment is led by the Royal Belgian Institute for Space Aeronomy (IASB-BIRA), assisted by Co-PI teams from Spain (IAA-CSIC), Italy (INAF-IAPS), and the United Kingdom (Open University). This project acknowledges funding by the Belgian Science Policy Office (BELSPO), with the financial and contractual coordination by the ESA Prodex Office (PEA 4000103401, 4000121493), by Spanish Ministry of Science and Innovation (MCIU) and by European funds under grants PGC2018-101836-B-I00 and ESP2017-87143-R (MINECO/FEDER), as well as by UK Space Agency through grants ST/V002295/1, ST/V005332/1, ST/Y000234/1 and ST/X006549/1 and Italian Space Agency through Grant 2018-2-HH.0. This project has received funding from the European Union's Horizon 2020 research and innovation program under grant agreement No 101004052. US investigators were supported by the National Aeronautics and Space Administration. Canadian investigators were supported by the Canadian Space Agency. This work was supported by the Institute for Basic Science (IBS-R035-C1). We want to thank M. Vals, F. Montmessin, F. Lefevre and the broad team supporting the continuous development of the Mars PCM.

References

Alday, J., Trokhimovskiy, A., Irwin, P. G., Wilson, C. F., Montmessin, F., Lefèvre, F., et al. (2021). Isotopic fractionation of water and its photolytic products in the atmosphere of Mars. *Nature Astronomy*, *5*(9), 943–950. https://doi.org/10.1038/s41550-021-01389-x

Aoki, S., Vandaele, A., Daerden, F., Villanueva, G. L., Liuzzi, G., Clancy, R., et al. (2022). Global vertical distribution of water vapor on Mars: Results from 3.5 years of ExoMars-TGO/NOMAD science operations. *Journal of Geophysical Research: Planets*, *127*(9), e2022JE007231. https://doi.org/10.1029/2022JE007231

Aoki, S., Vandaele, A. C., Daerden, F., Villanueva, G. L., Liuzzi, G., Thomas, I. R., et al. (2019). Water vapor vertical profiles on Mars in dust storms observed by TGO/NOMAD. *Journal of Geophysical Research: Planets*, *124*(12), 3482–3497. https://doi.org/10.1029/2019JE006109

Barnes, J. R., Haberle, R. M., Wilson, R. J., Lewis, S., Murphy, J. R., & Read, P. L. (2017). The global circulation.

Belyaev, D. A., Fedorova, A., Trokhimovskiy, A., Alday, J., Montmessin, F., Korablev, O. I., et al. (2021). Revealing a high water abundance in the upper mesosphere of Mars with ACS onboard TGO. *Geophysical Research Letters*, *48*(10), e2021GL093411. https://doi.org/10.1029/2021GL093411

Belyaev, D. A., Fedorova, A. A., Trokhimovskiy, A., Alday, J., Korablev, O. I., Montmessin, F., et al. (2022). Thermal structure of the middle and upper atmosphere of Mars from ACS/TGO CO2 spectroscopy. *Journal of Geophysical Research: Planets*, *127*(10), e2022JE007286. https://doi.org/10.1029/2022JE007286

Bertaux, J.-L., Nevejans, D., Korablev, O., Villard, E., Quémerais, E., Neefs, E., et al. (2007). SPICAV on Venus express: Three spectrometers to study the global structure and composition of the Venus atmosphere. *Planetary and Space Science*, *55*(12), 1673–1700. https://doi.org/10.1016/j.pss.2007.01.016

Brines, A. (2025). Water vapor vertical distribution on Mars after six years of TGO/NOMAD solar occultations [Dataset]. *Part I: Global Climatology*. https://doi.org/10.5281/zenodo.15146458

Brines, A., López-Valverde, M., Funke, B., González-Galindo, F., Aoki, S., Villanueva, G., et al. (2024). Strong localized pumping of water vapor to high altitudes on Mars during the perihelion season. *Geophysical Research Letters*, *51*(14), e2023GL107224. https://doi.org/10.1029/2023GL107224

Brines, A., López-Valverde, M., Stolzenbach, A., Modak, A., Funke, B., Galindo, F., et al. (2023). Water vapor vertical distribution on Mars during perihelion season of MY 34 and MY 35 with ExoMars-TGO/NOMAD observations. *Journal of Geophysical Research: Planets*, *128*(11), e2022JE007273. https://doi.org/10.1029/2022JE007273

Chaffin, M., Kass, D., Aoki, S., Fedorova, A., Deighan, J., Connour, K., et al. (2021). Martian water loss to space enhanced by regional dust storms. *Nature Astronomy*, *5*(10), 1036–1042. https://doi.org/10.1038/s41550-021-01425-w

Clancy, R. T., Sandor, B. J., Wolff, M. J., Smith, M. D., Lefèvre, F., Madeleine, J.-B., et al. (2012). Extensive MRO CRISM observations of 1.27 μm O_2 airglow in Mars polar night and their comparison to MRO MCS temperature profiles and LMD GCM simulations. *Journal of Geophysical Research*, *117*(E11), E00J10. https://doi.org/10.1029/2011JE004018

Clancy, R. T., Wolff, M. J., Smith, M. D., Kleinböhl, A., Cantor, B. A., Murchie, S. L., et al. (2019). The distribution, composition, and particle properties of mars mesospheric aerosols: An analysis of CRISM visible/near-IR limb spectra with context from near-coincident MCS and MARCI observations. *Icarus*, *328*, 246–273. https://doi.org/10.1016/j.icarus.2019.03.025

von Clarmann, v., Glatthor, N., Grabowski, U., Höpfner, M., Kellmann, S., Kiefer, M., et al. (2003). Retrieval of temperature and tangent altitude pointing from limb emission spectra recorded from space by the michelson interferometer for passive atmospheric sounding (MIPAS). *Journal of Geophysical Research*, *108*(D23), 4736. https://doi.org/10.1029/2003jd003602

Daerden, F., Whiteway, J., Davy, R., Verhoeven, C., Komguem, L., Dickinson, C., et al. (2010). Simulating observed boundary layer clouds on Mars. *Geophysical Research Letters*, *37*(4), L04203. https://doi.org/10.1029/2009GL041523

ESA. (2024a). *EAICD*. European Space Agency. Retrieved from https://archives.esac.esa.int/psa/ftp/ExoMars2016/em16_tgo_nmd/document/EAICD/

ESA. (2024b). *PSA*. European Space Agency. Retrieved from https://archives.esac.esa.int/psa/

Fedorova, A., Bertaux, J.-L., Betsis, D., Montmessin, F., Korablev, O., Maltagliati, L., & Clarke, J. (2018). Water vapor in the middle atmosphere of Mars during the 2007 global dust storm. *Icarus*, *300*, 440–457. https://doi.org/10.1016/j.icarus.2017.09.025

Fedorova, A., Korablev, O., Bertaux, J.-L., Rodin, A., Montmessin, F., Belyaev, D., & Reberac, A. (2009). Solar infrared occultation observations by SPICAM experiment on Mars-Express: Simultaneous measurements of the vertical distributions of H_2O, CO_2 and aerosol. *Icarus*, *200*(1), 96–117. https://doi.org/10.1016/j.icarus.2008.11.006

Fedorova, A., Montmessin, F., Korablev, O., Lefèvre, F., Trokhimovskiy, A., & Bertaux, J.-L. (2021). Multi-annual monitoring of the water vapor vertical distribution on Mars by SPICAM on Mars Express. *Journal of Geophysical Research: Planets*, *126*(1), e2020JE006616. https://doi.org/10.1029/2020je006616

Fedorova, A., Montmessin, F., Korablev, O., Luginin, M., Trokhimovskiy, A., Belyaev, D. A., et al. (2020). Stormy water on Mars: The distribution and saturation of atmospheric water during the dusty season. *Science*, *367*(6475), 297–300. https://doi.org/10.1126/science.aay9522

Fedorova, A., Montmessin, F., Trokhimovskiy, A., Luginin, M., Korablev, O., Alday, J., et al. (2023). A two-martian years survey of the water vapor saturation state on Mars based on ACS NIR/TGO occultations. *Journal of Geophysical Research: Planets*, *128*(1), e2022JE007348. https://doi.org/10.1029/2022je007348

Forget, F., Hourdin, F., Fournier, R., Hourdin, C., Talagrand, O., Collins, M., et al. (1999). Improved general circulation models of the Martian atmosphere from the surface to above 80 km. *Journal of Geophysical Research*, *104*(E10), 24155–24175. https://doi.org/10.1029/1999je001025

Haberle, R. M., Kahre, M. A., Hollingsworth, J. L., Montmessin, F., Wilson, R. J., Urata, R. A., et al. (2019). Documentation of the NASA/AMES legacy mars global climate model: Simulations of the present seasonal water cycle. *Icarus*, *333*, 130–164. https://doi.org/10.1016/j.icarus.2019.03.026

Hernández-Bernal, J., Sánchez-Lavega, A., del Río-Gaztelurrutia, T., Hueso, R., Ravanis, E., Cardesín-Moinelo, A., et al. (2021). A long-term study of mars mesospheric clouds seen at twilight based on mars express VMC images. *Geophysical Research Letters*, *48*(7), e2020GL092188. https://doi.org/10.1029/2020gl092188

Holmes, J., Lewis, S., Patel, M., Chaffin, M., Cangi, E., Deighan, J., et al. (2021). Enhanced water loss from the Martian atmosphere during a regional-scale dust storm and implications for long-term water loss. *Earth and Planetary Science Letters*, *571*, 117109. https://doi.org/10.1016/j.epsl.2021.117109

Holsclaw, G. M., Deighan, J., Almatroushi, H., Chaffin, M., Correira, J., Evans, J. S., et al. (2021). The emirates Mars ultraviolet spectrometer (EMUS) for the EMM mission. *Space Science Reviews*, *217*, 1–49. https://doi.org/10.1007/s11214-021-00854-3

Kass, D., Kleinböhl, A., McCleese, D., Schofield, J., & Smith, M. (2016). Interannual similarity in the Martian atmosphere during the dust storm season. *Geophysical Research Letters*, *43*(12), 6111–6118. https://doi.org/10.1002/2016gl068978

Kass, D., Schofield, J., Kleinböhl, A., McCleese, D., Heavens, N., Shirley, J., & Steele, L. (2020). Mars Climate Sounder observation of Mars' 2018 global dust storm. *Geophysical Research Letters*, *47*(23), e2019GL083931. https://doi.org/10.1029/2019gl083931

Korablev, O., Montmessin, F., Trokhimovskiy, A., Fedorova, A. A., Shakun, A., Grigoriev, A., et al. (2018). The atmospheric chemistry suite (ACS) of three spectrometers for the ExoMars 2016 Trace gas orbiter. *Space Science Reviews*, *214*, 1–62. https://doi.org/10.1007/s11214-017-0437-6

Liuzzi, G., Villanueva, G. L., Crismani, M. M., Smith, M. D., Mumma, M. J., Daerden, F., et al. (2020). Strong variability of Martian water ice clouds during dust storms revealed from ExoMars Trace Gas Orbiter/NOMAD. *Journal of Geophysical Research: Planets*, *125*(4), e2019JE006250. https://doi.org/10.1029/2019je006250

Liuzzi, G., Villanueva, G. L., Mumma, M. J., Smith, M. D., Daerden, F., Ristic, B., et al. (2019). Methane on Mars: New insights into the sensitivity of CH4 with the NOMAD/ExoMars spectrometer through its first in-flight calibration. *Icarus*, *321*, 671–690. https://doi.org/10.1016/j.icarus.2018.09.021

López-Valverde, M. A., Funke, B., Brines, A., Stolzenbach, A., Modak, A., Hill, B., et al. (2023). Martian atmospheric temperature and density profiles during the first year of NOMAD/TGO solar occultation measurements. *Journal of Geophysical Research: Planets*, *128*(2), e2022JE007278. https://doi.org/10.1029/2022je007278

Maltagliati, L., Montmessin, F., Fedorova, A., Korablev, O., Forget, F., & Bertaux, J.-L. (2011). Evidence of water vapor in excess of saturation in the atmosphere of Mars. *Science*, *333*(6051), 1868–1871. https://doi.org/10.1126/science.1207957

Maltagliati, L., Montmessin, F., Korablev, O., Fedorova, A., Forget, F., Määttänen, A., et al. (2013). Annual survey of water vapor vertical distribution and water–Aerosol coupling in the Martian atmosphere observed by SPICAM/MEX solar occultations. *Icarus*, *223*(2), 942–962. https://doi.org/10.1016/j.icarus.2012.12.012

Martín-Rubio, C., Vicente-Retortillo, A., Gómez, F., & Rodríguez-Manfredi, J. (2024). Interannual variability of regional dust storms between Mars years 24 and 36. *Icarus*, *412*, 115982. https://doi.org/10.1016/j.icarus.2024.115982

McCleese, D., Heavens, N., Schofield, J., Abdou, W., Bandfield, J., Calcutt, S., et al. (2010). Structure and dynamics of the Martian lower and middle atmosphere as observed by the Mars climate sounder: Seasonal variations in zonal mean temperature, dust, and water ice aerosols. *Journal of Geophysical Research*, *115*(E12), E12016. https://doi.org/10.1029/2010je003677

Medvedev, A. S., & Hartogh, P. (2007). Winter polar warmings and the meridional transport on Mars simulated with a general circulation model. *Icarus*, *186*(1), 97–110. https://doi.org/10.1016/j.icarus.2006.08.020

Modak, A., López-Valverde, M. A., Brines, A., Stolzenbach, A., Funke, B., González-Galindo, F., et al. (2023). Retrieval of Martian atmospheric CO vertical profiles from NOMAD observations during the first year of TGO operations. *Journal of Geophysical Research: Planets*, *128*(3), e2022JE007282. https://doi.org/10.1029/2022je007282

Montabone, L., Spiga, A., Kass, D. M., Kleinböhl, A., Forget, F., & Millour, E. (2020). Martian year 34 column dust climatology from Mars climate sounder observations: Reconstructed maps and model simulations. *Journal of Geophysical Research: Planets*, *125*(8), e2019JE006111. https://doi.org/10.1029/2019je006111

Neary, L., Daerden, F., Aoki, S., Whiteway, J., Clancy, R. T., Smith, M., et al. (2020). Explanation for the increase in high-altitude water on Mars observed by NOMAD during the 2018 global dust storm. *Geophysical Research Letters*, *47*(7), e2019GL084354. https://doi.org/10.1029/2019gl084354

Neefs, E., Vandaele, A. C., Drummond, R., Thomas, I. R., Berkenbosch, S., Clairquin, R., et al. (2015). NOMAD spectrometer on the ExoMars trace gas orbiter mission: Part 1—Design, manufacturing and testing of the infrared channels. *Applied optics*, *54*(28), 8494–8520. https://doi.org/10.1364/ao.54.008494

Pankine, A. A. (2022). Martian atmospheric water vapor abundances in my26-30 from mars express PFS/LW observations. *Icarus*, *379*, 114975. https://doi.org/10.1016/j.icarus.2022.114975

Pankine, A. A., Leung, C., Tamppari, L., Martinez, G., Giuranna, M., Piqueux, S., et al. (2023). Effects of global dust storms on water vapor in the southern polar region of Mars. *Journal of Geophysical Research: Planets*, *128*(12), e2023JE008016. https://doi.org/10.1029/2023je008016

Richardson, M. I., & Wilson, R. J. (2002). A topographically forced asymmetry in the Martian circulation and climate. *Nature*, *416*(6878), 298–301. https://doi.org/10.1038/416298a

Rodin, A., Korablev, O., & Moroz, V. (1997). Vertical distribution of water in the near-equatorial troposphere of Mars: Water vapor and clouds. *Icarus*, *125*(1), 212–229. https://doi.org/10.1006/icar.1996.5602

Shaposhnikov, D. S., Medvedev, A. S., Rodin, A. V., & Hartogh, P. (2019). Seasonal water "pump" in the atmosphere of Mars: Vertical transport to the thermosphere. *Geophysical Research Letters*, *46*(8), 4161–4169. https://doi.org/10.1029/2019gl082839

Smith, M. D. (2002). The annual cycle of water vapor on Mars as observed by the Thermal Emission Spectrometer. *Journal of Geophysical Research*, *107*(E11), 251. https://doi.org/10.1029/2001je001522

Smith, M. D. (2004). Interannual variability in TES atmospheric observations of Mars during 1999–2003. *Icarus*, *167*(1), 148–165. https://doi.org/10.1016/j.icarus.2003.09.010

Smith, M. D. (2019). Local time variation of water ice clouds on mars as observed by THEMIS. *Icarus*, *333*, 273–282. https://doi.org/10.1016/j.icarus.2019.06.009

Smith, M. D., Bougher, S. W., Encrenaz, T., Forget, F., & Kleinböhl, A. (2017). Thermal structure and composition. *The Atmosphere and Climate of Mars*, *18*, 42. https://doi.org/10.1017/9781139060172.004

Stcherbinine, A., Montmessin, F., Vincendon, M., Wolff, M. J., Vals, M., Korablev, O., et al. (2022). A two martian years survey of water ice clouds on mars with ACS onboard TGO. *Journal of Geophysical Research: Planets*, *127*(12), e2022JE007502. https://doi.org/10.1029/2022je007502

Stiller, G. P. (2000). The karlsruhe optimized and precise radiative transfer Algorithm (KOPRA).

Stolzenbach, A., López Valverde, M.-A., Brines, A., Modak, A., Funke, B., González-Galindo, F., et al. (2023). Martian atmospheric aerosols composition and distribution retrievals during the first Martian year of NOMAD/TGO solar occultation measurements: 1. Methodology and application to the MY 34 global dust storm. *Journal of Geophysical Research: Planets*, *128*(11), e2022JE007276. https://doi.org/10.1029/2022je007276

Streeter, P. M., Lewis, S. R., Patel, M. R., Holmes, J. A., Fedorova, A. A., Kass, D. M., & Kleinböhl, A. (2021). Asymmetric impacts on Mars' polar vortices from an equinoctial global dust storm. *Journal of Geophysical Research: Planets*, *126*(5), e2020JE006774. https://doi.org/10.1029/2020je006774

Thomas, I. R., Aoki, S., Trompet, L., Robert, S., Depiesse, C., Willame, Y., et al. (2022). Calibration of NOMAD on ESA's ExoMars trace gas orbiter: Part 1–the solar occultation channel. *Planetary and Space Science*, *218*, 105411. https://doi.org/10.1016/j.pss.2021.105411

Trompet, L., Vandaele, A., Thomas, I., Aoki, S., Daerden, F., Erwin, J., et al. (2023). Carbon dioxide retrievals from NOMAD-SO on ESA's ExoMars trace gas orbiter and temperature profiles retrievals with the hydrostatic equilibrium equation: 1. Description of the method. *Journal of Geophysical Research: Planets*, *128*(3), e2022JE007277. https://doi.org/10.1029/2022je007277

Vandaele, A. C., Korablev, O., Daerden, F., Aoki, S., Thomas, I. R., Altieri, F., et al. (2019). Martian dust storm impact on atmospheric H_2O and D/H observed by ExoMars Trace Gas Orbiter. *Nature*, *568*(7753), 521–525. https://doi.org/10.1038/s41586-019-1097-3

Vandaele, A. C., Lopez-Moreno, J.-J., Patel, M. R., Bellucci, G., Daerden, F., Ristic, B., et al. (2018). NOMAD, an integrated suite of three spectrometers for the ExoMars trace gas mission: Technical description, science objectives and expected performance. *Space Science Reviews*, *214*(5), 1–47. https://doi.org/10.1007/s11214-018-0517-2

Villanueva, G., Mumma, M., Novak, R., Käufl, H., Hartogh, P., Encrenaz, T., et al. (2015). Strong water isotopic anomalies in the Martian atmosphere: Probing current and ancient reservoirs. *Science*, *348*(6231), 218–221. https://doi.org/10.1126/science.aaa3630

Villanueva, G. L., Liuzzi, G., Aoki, S., Stone, S. W., Brines, A., Thomas, I. R., et al. (2022). The deuterium isotopic ratio of water released from the Martian caps as measured with TGO/NOMAD. *Geophysical Research Letters*, *49*(12), e2022GL098161. https://doi.org/10.1029/2022gl098161

Villanueva, G. L., Liuzzi, G., Crismani, M. M., Aoki, S., Vandaele, A. C., Daerden, F., et al. (2021). Water heavily fractionated as it ascends on Mars as revealed by ExoMars/NOMAD. *Science Advances*, *7*(7), eabc8843. https://doi.org/10.1126/sciadv.abc8843